Expansion of the 4D XCAT Phantom Library with Anatomical Texture

by

Jason Dale Bond

Graduate Progam in Medical Physics
Duke University

Date:_____

Approved:

_____
Ehsan Samei, Supervisor

_____
William Paul Segars

_____
Robert Reiman

_____
James Dobbins

Thesis submitted in partial fulfillment of
the requirements for the degree of Master of Science in the
Graduate Program in Medical Physics in
the Graduate School of
Duke University

2013

ABSTRACT

Expansion of the 4D XCAT Phantom Library with Anatomical Texture

by

Jason Dale Bond

Graduate Program in Medical Physics
Duke University

Date:_____
Approved:

_____
Ehsan Samei, Supervisor

_____
William Paul Segars

_____
Robert Reiman

_____
James Dobbins

An abstract of a thesis submitted in partial fulfillment of
the requirements for the degree of Master of Science in
the Graduate Program in Medical Physics in
the Graduate School of
Duke University

2013

Abstract

Computational phantoms are set to play an important role in imaging research. As medicine moves increasingly towards providing individualized, patient-specific care, it is imperative that simulations be completed on patient-specific anatomy, rather than a reference standard. To that end, there is need for a variety of realistic phantoms for clinical studies.

This work adds to the existing extended cardiac and torso (XCAT) adult phantom series (two phantoms based on visual human data) by building new models based on adult patient computed tomography (CT) image data. These CT datasets were obtained from Duke University's patient CT database.

Each image-set was segmented using in-house segmentation software, defining bony structures and large organs within the field of view. 3D non-uniform rational b-spline (NURBS) surfaces were fitted to the segmented data. Using the multi-channel large diffeomorphic deformation metric mapping (MC-LDDMM) network, a transform was calculated to morph an existing XCAT model to the segmented patient geometry. Fifty-eight adult XCAT models were added to the phantom library.

In addition to the expanding the XCAT library, the feasibility of incorporating texture was investigated. Currently, the XCAT phantom structures are assumed to be homogeneous. This can lead to unrealistic appearance when the phantoms are combined

with imaging simulations, particularly in CT. The purpose of this project was to capture anatomical texture and test it in a simulated phantom. Image data from the aforementioned patient CT database served as the source of anatomical texture.

The images were de-noised using anisotropic diffusion. Next, several regions of interest (ROIs) were taken from the liver and lungs of CT images. Using the ROIs as a source of texture, a larger stochastic texture image-set was created using the Image Quilting algorithm.

The visual human adult male XCAT phantom was voxelized at the same resolution as the texture image. The voxels inside the liver were directly replaced by the corresponding voxels of texture. Similarly for the lung, the voxels between the existing lung bronchi/blood vessels and the lung wall were replaced by texture voxels. This procedure was performed using ten different patient CT image-sets as sources of texture.

To validate the similarity of the artificial textures to the source textures, reconstructions of the adult male XCAT phantom with added textures were compared to the clinical images via receiver operator characteristic (ROC) analysis, a two-sample t-test, equivalence test, and through comparing absolute differences between scores.

It was concluded that this framework provides a valuable tool in which anatomical texture can be incorporated into computational phantoms. It is anticipated that this step towards making many anatomically variable virtual models indicative of a

patient populace and making these models more realistic will be useful in medical imaging research, especially for studies relating to image quality.

Contents

Abstract iv

List of Tables ix

List of Figures x

Acknowledgements xii

1. Introduction 1

2. Part One: Expansion of the XCAT library 2

2.1 Phantom Background 2

2.1.1 Need for realistic and variable phantoms 2

2.1.2 Previous work 3

2.2 Methods 6

2.2.1 Four steps to create an XCAT phantom 6

2.2.1.1 Building the initial model 7

2.2.1.2 Calculate the LDDMM transform 8

2.2.1.3 Apply the LDDMM transform 11

2.2.1.4 Finalize the phantom 11

2.3 Results 13

2.4 Discussion 18

3. Part Two: Simulating anatomical texture for virtual human model 20

3.1 Background 20

3.2 Methods 22

3.2.1 Texture Preparation 22
3.2.2 Texture Extraction 24
3.2.3 Texture Extrapolation 26
3.2.4 Texture Transfer 28
3.2.5 Phantom Simulation 28
3.2.6 Texture Evaluation 29
3.3 Results 32
3.3.1 T-tests 32
3.3.2 ROC analysis 32
3.3.3 Equivalence tests 35
3.3.4 Score differences 36
3.4 Discussion 38
4. Conclusions 43
References 45

List of Tables

Table 1: Mean and standard deviation of the organ masses of the adult models as compared with the organ masses from ICRP 89 17

Table 2: Summary of t-test results comparing mean scores of simulated and real textures. The threshold of significance was 0.05; below which, results were considered statistically significant. 34

Table 3: The area under the ROC curve (AUC) served as a metric for realism. An AUC value of 0.5 implies that simulated textures were indistinguishable from real textures. . 34

List of Figures

Figure 1: 4D XCAT phantom. The male and female anatomies are shown above. 3D renderings of the male phantom are shown to illustrate the cardiac and respiratory motions. 3

Figure 2: The XCAT phantom can be used for multiple modality imaging. Shown is a non-textured XCAT phantom that was used in conjunction with imaging simulators to generate imaging data. Note that for CT the difference between simulated data (left column) and patient data (right column) is quite apparent. Image taken from Segars et. al.[10] 4

Figure 3: BMI and ages of the patients used in developing XCAT phantoms. 7

Figure 4: ImageSegment, a GUI developed in our lab, allowed for manual segmentation of critical structures. 8

Figure 5: Procedure for calculating the MC-LDDMM transform. To calculate the MC-LDDMM transform, template and target images are required. The above steps are performed to create these images. 10

Figure 6: The MC-LDDMM transform is used to transform the template XCAT phantom to define the detailed anatomy of the patient. 11

Figure 7: Collage showing the 58 new adult anatomies. The head, arms, and legs are not shown to focus on the chest-abdomen-pelvis anatomy, which is based on the patient imaging data. The muscles and blood vessels are also not shown for presentation purposes. 14

Figure 8: Four adult female XCAT phantoms (top) with CT simulation results (bottom). 15

Figure 9: Using a diffusion technique, the patient images were smoothed until the power spectra density in the liver was reduced to 50%. 24

Figure 10: An ensemble of ROIs taken from CT images of a patient's lung serves as input for the Image Quilting algorithm which was used to create textures. 26

Figure 11: Top - The Image Quilting algorithm is graphically illustrated. Bottom - Larger images can be generated from a smaller sized texture source. 27

Figure 12: Once a large texture image is generated, it is combined with a voxelized XCAT phantom to produce a more realistic appearing model. 28

Figure 13: Using our methods, computational phantoms can move from surface defined structures (left) to filling in structures with patient-informed texture (right)..... 29

Figure 14: ROIs of different sizes were displayed at 120x120 pixels before observers. Left, lung textures from simulated and real cases are displayed. Right, liver textures from simulated and real cases are shown. 30

Figure 15: Results of the receiver operator (ROC) analysis showing true positive rate plotted against false positive rate. Textures from real patients were considered positive cases. Responses from lung textures are above and liver textures are below. 35

Figure 16: Results from the equivalence test based on the 95% confidence interval of $\Delta\bar{\mu}$ (difference of mean scores between real texture and artificial texture). The equivalence zone was defined as $\pm\boldsymbol{\sigma}_{\mathbf{real}}$, the standard deviation of real texture scores averaged across observers..... 36

Acknowledgements

I would like to express gratitude for guidance and support rendered by my advisors, Dr. Samei and Dr. Segars. Without which, I would not have been able to undertake this work. Their optimism and encouragement has sustained me through my dark moments. I also extend my thanks to the other members of my committee, Dr. Dobbins and Dr. Reiman, and my fellow lab-mates within RAI Labs, who have also given much needed help and support. Without which, I would not have been able to *complete* this work.

I also want to take this moment and extend a heartfelt token of gratitude to my son, Rogan. The timing of your arrival into our home and hearts could not have been more appropriate. Rogan, you have changed me forever; your entrance into this world filled me with a certain peace that has stayed ever since. You bring renewed purpose and validity to everything I do.

Mostly, I want to acknowledge my dearest companion of the last five years and for forever – my exemplar, my friend, my confidant, my wife, Shayla. I cannot imagine going through this struggle alone; you somehow manage to consistently satiate the soul's sincerest yearnings; home, faith, love, to name a few. May our marriage grow to withstand the perils of life and the refining fires of eternity.

1. Introduction

This work is divided into two parts; the first is the expansion of the XCAT library of adult phantoms. Part one considers the necessity for and creation of an adult series of computational phantoms and is reflected in SPIE proceedings and the journal *Medical Physics*[1, 2]. Part two of this document is towards simulating anatomical texture for virtual human models and is reflected in further SPIE proceedings[3] and was submitted for publication in *Transactions in Medical Imaging*.

2. Part One: Expansion of the XCAT library

2.1 Phantom Background

Computational phantoms are finding a wide use in medical imaging research[4-8]. Given radiation concerns with patients and the expense of physical phantoms, computational phantoms provide the only practical technique with which to optimize CT applications and protocols. Combined with accurate models of the imaging process, phantoms can be used to simulate imaging data as if they were actual patients. They can be imaged repeatedly under many different scanning conditions and parameters without any fear of radiation exposure. Effects of acquisition parameters, physical processes and patient anatomy and motion can all be separated out (holding other parameters constant) and studied or compensated for independently. With a limited number of physical phantoms available, computational phantoms also have the greatest potential to estimate patient-specific organ and effective dose in CT by providing a library of anatomically diverse models from which to best derive these values.

2.1.1 Need for realistic and variable phantoms

In order for computerized phantoms to be useful, they must be very realistic or the data simulated from them will not be indicative of what would occur in live patients. To date, the most realistic phantoms are based on the segmentation of patient imaging data, typically MRI or CT[9]. Segmentation of patient data is a time-consuming process that can take many months to a year to complete. As a result, only a handful of realistic

computational models currently exist, most being limited to 3D and not modeling patient motion. In order to more closely mimic a clinical study or trial, a large population of phantoms is needed that includes a range of anatomical variations representative of the public at large.

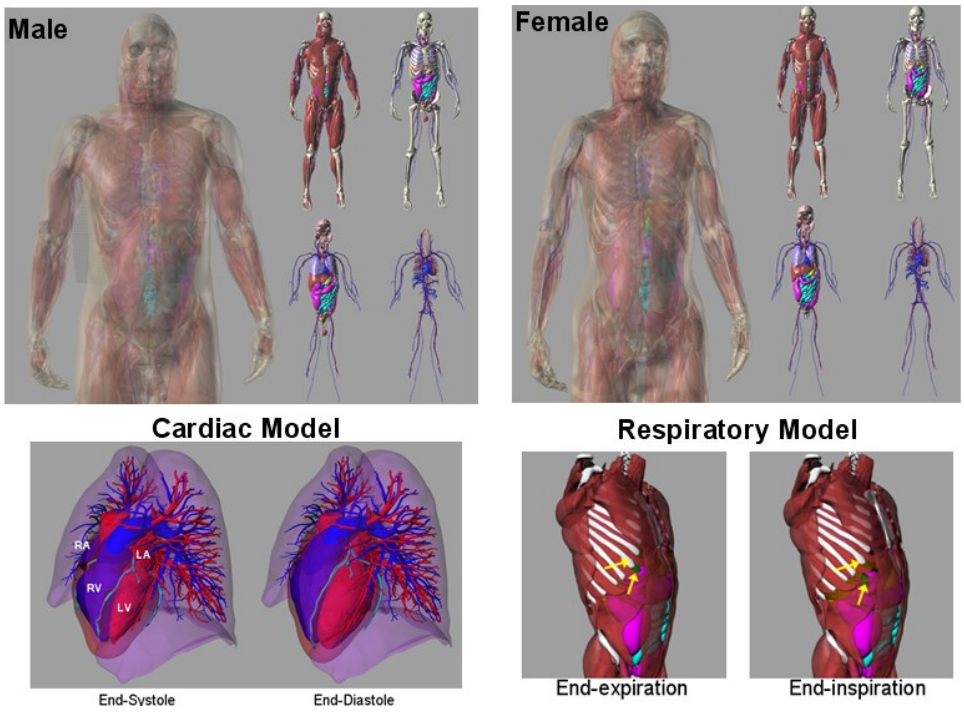

Figure 1: 4D XCAT phantom. The male and female anatomies are shown above. 3D renderings of the male phantom are shown to illustrate the cardiac and respiratory motions.

2.1.2 Previous work

We developed the 4D extended cardiac-torso (XCAT) phantom[10] with the purpose of applying it to high-resolution CT research to optimize 3D and 4D CT applications in terms of image quality and radiation dose. The 4D XCAT consists of whole-body adult male and female models which contain an unmatched level of detail

and anatomical realism (Fig. 1). The male and female anatomies were based on the Visible Human anatomical imaging data. The XCAT includes parameterized models for the cardiac and respiratory motions based on gated patient imaging data. The XCAT phantoms are extremely realistic, containing thousands of anatomical structures. These phantoms may be used in multiple imaging modalities (Fig. 2). Like other computational phantoms, however, a drawback to the XCAT is that it is limited to just a few anatomies, in this case the adult male and female.

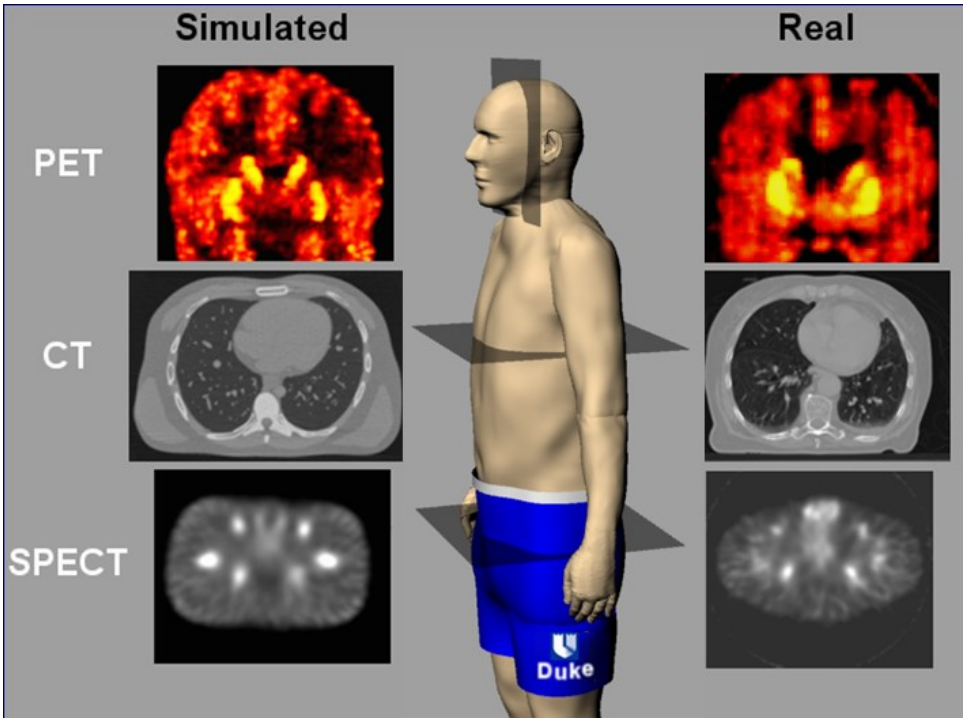

Figure 2: The XCAT phantom can be used for multiple modality imaging. Shown is a non-textured XCAT phantom that was used in conjunction with imaging simulators to generate imaging data. Note that for CT the difference between simulated data (left column) and patient data (right column) is quite apparent. Image taken from Segars et. al.[10]

In previous work[11], we developed an innovative method to efficiently create highly detailed, full-body patient-specific phantoms by morphing the XCAT phantom to match patient imaging data. We used this method to create 42 pediatric XCAT phantoms ranging in age from 8 weeks to 12 years old. In this work, we apply the same method to create a new series of 58 adult XCAT models of varying ages and weights. Combined with the pediatric models, we now have a population of 100 phantoms for use in imaging research.

2.2 Methods

2.2.1 Four steps to create an XCAT phantom

There are four steps to building a patient-specific XCAT phantom; segmentation, building an initial base model, calculating and applying the Multi-Channel Large Deformation Diffeomorphic Metric Mapping (MC-LDDMM) transform from the XCAT to the patient framework, and finalization. First, patient datasets were collected from the Duke University CT imaging database. Chest-abdomen-pelvis (CAP) datasets were obtained to represent a wide range of body types for both adult males and adult females as determined by their age and weight percentile (Fig. 2). Manual segmentation of selected organs was performed using ImageSegment, a custom graphical application developed in our laboratory (Fig. 3). The segmentation was performed on a tablet monitor with a light pen to make it easier to segment and define critical structures.

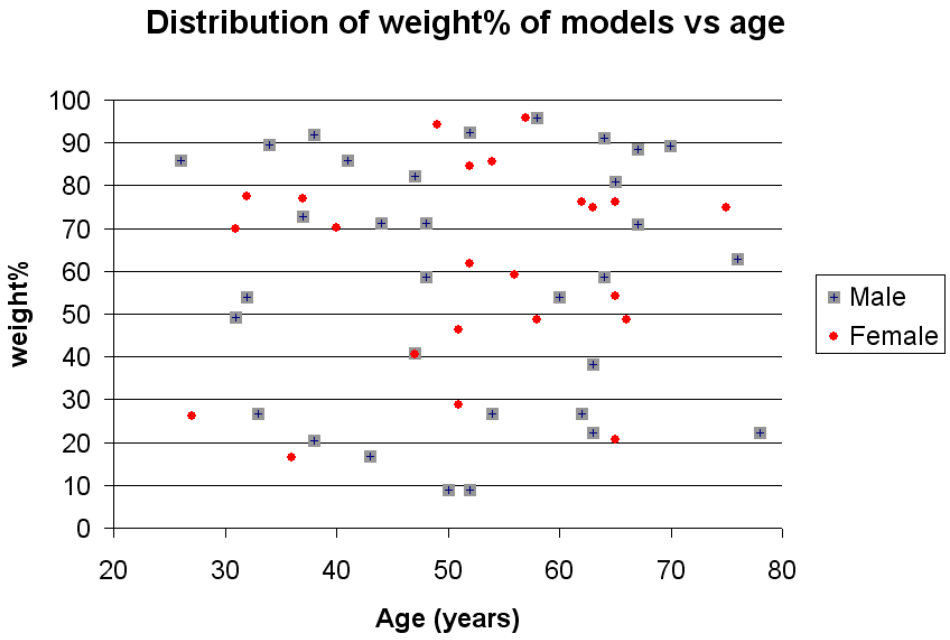

Figure 3: Weight percentile and ages of the patients used in developing XCAT phantoms.

2.2.1.1 Building the initial model

The initial patient model was constructed by fitting 3D polygon mesh surfaces to the segmented organs and structures (e.g. body surface, backbone, ribs, lungs, liver, heart, stomach, spleen, gallbladder, bladder, etc.). Within ImageSegment, each segmented structure was outputted as a 3D polygon model using the marching cubes algorithm from the Visualization Toolkit (VTK), www.vtk.org. The polygon models were imported into the Rhinoceros NURBS modeling software, www.rhino3d.com, and cubic NURBS surfaces were fitted to them creating an initial NURBS-based patient model. This initial model only covered the chest, abdomen, and pelvis region. To complete the phantom, we manually added on the head, arms, and legs using an

existing male or female full-body XCAT template model selected to best match the age and anatomy of the patient.

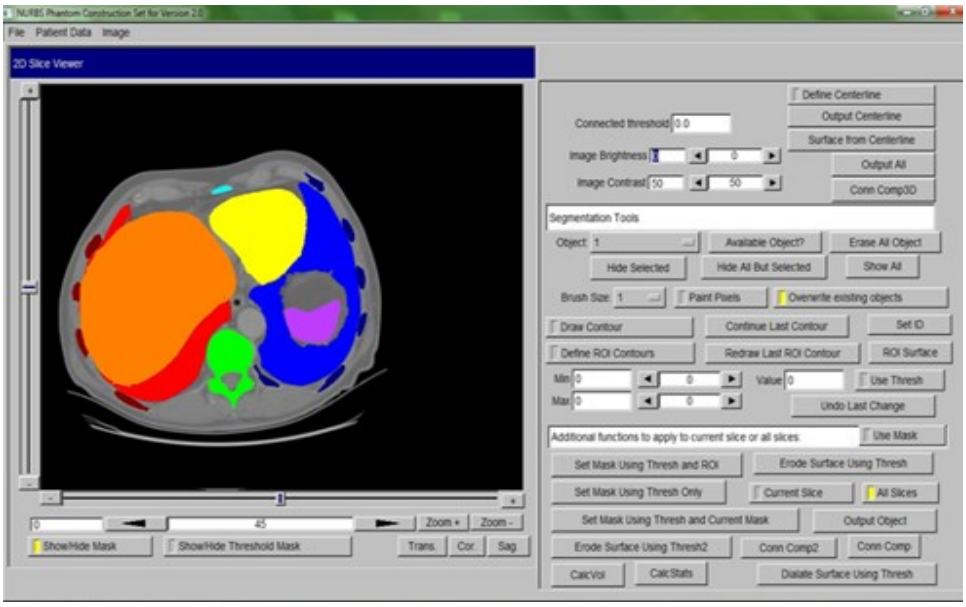

Figure 4: ImageSegment, a GUI developed in our lab, allowed for manual segmentation of critical structures.

2.2.1.2 Calculate the LDDMM transform

Once the initial patient model was constructed, the MC-LDDMM framework[12-14], developed by Dr. Michael Miller's group in the Center for Imaging Science at the Johns Hopkins University, was used to fill in the rest of the anatomy by transforming the selected template XCAT phantom (Visible Human-based male or female) to match the limited framework defined for the target patient model.

To calculate the MC-LDDMM transform, images of the XCAT template and the patient target are required. The template and target images for each case were created by voxelizing the template and target models into 3D images covering the whole body.

Structures from the patient model were assigned a unique integer ID in the target image to drive the MC-LDDMM transform. The template model was set to contain the same structures and intensities as the target so the models have a 1:1 correspondence. Landmarks were defined using the template and target skeletons. Corresponding landmarks were placed on the endpoints of bones such as the ribs, arm/leg bones, and sternum. The spinal processes also served as landmarks. Given the selected landmarks and the template and target models, the data were sent to Dr. Michael Miller's group where the MC-LDDMM method calculated the high level transform to map the whole-body template (XCAT) to the target (patient framework). Figure 4 summarizes the steps to calculate the MC-LDDMM transform.

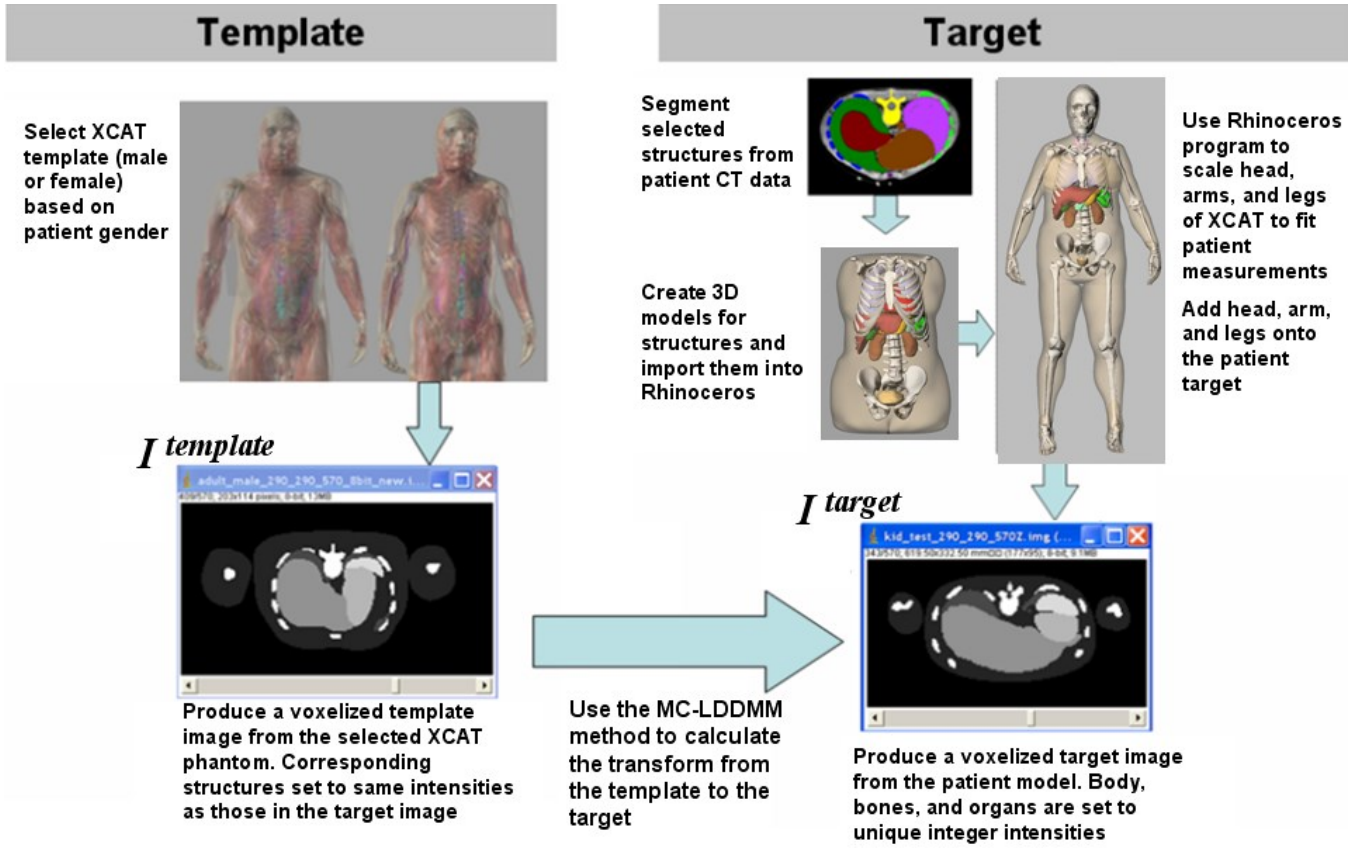

Figure 5: Procedure for calculating the MC-LDDMM transform. To calculate the MC-LDDMM transform, template and target images are required. The above steps are performed to create these images.

2.2.1.3 Apply the LDDMM transform

Once the transform was determined, it was applied to the template XCAT to create the patient-specific XCAT phantom containing all anatomical structures (Fig. 5). The MC-LDDMM transform was also applied to the base 4D cardiac model[10] of the XCAT to implement it in the new anatomy. The respiratory motion was modeled in each new phantom based on similar mechanics to that of the original XCAT[10].

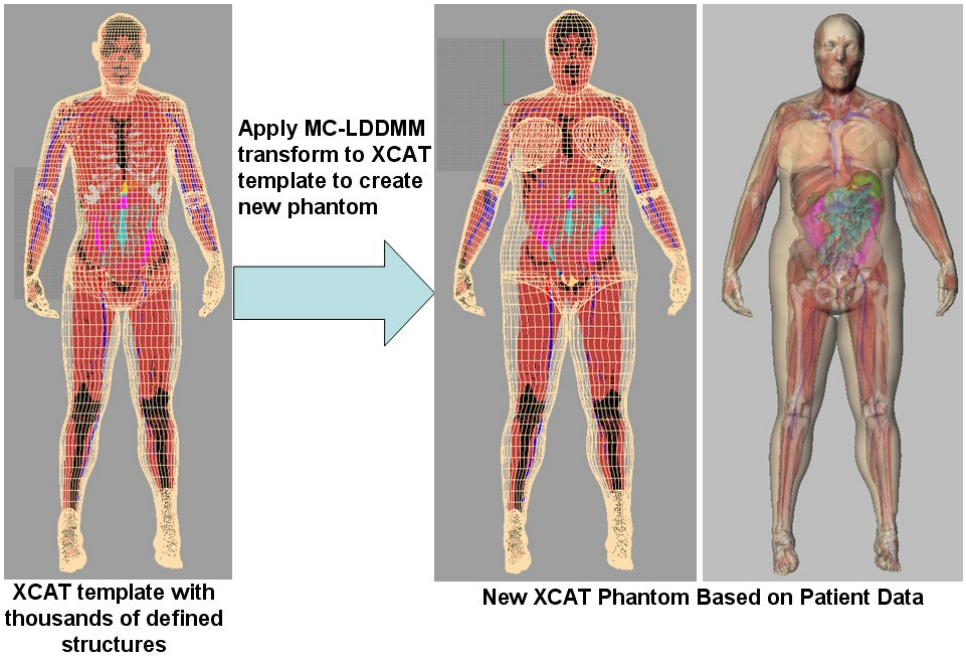

Figure 6: The MC-LDDMM transform is used to transform the template XCAT phantom to define the detailed anatomy of the patient.

2.2.1.4 Finalize the phantom

After receiving the transformed phantoms from Johns Hopkins, each new phantom was refined by checking for anatomical accuracy via visual inspection of the

3D models by Dr. Segars. If needed, minor adjustments were made. Using these methods, phantoms of multiple body types and sizes were created.

2.3 Results

Using our methods, we created a series of computerized phantoms with thousands of anatomical structures and modeling cardiac and respiratory motions. We created 58 (35 male and 23 female) anatomically variable phantoms in total (Fig. 6). These phantoms can be combined with existing simulation packages to simulate realistic imaging data. Figure 7 shows simulated CT data from 4 anatomically variable females. Clearly, these phantoms provide a means to obtain realistic-looking data. The advantage of having multiple shapes and sizes from an XCAT database allows for patient variability that would be common of a clinical trial.

This work provides a new population of 58 adult computerized phantoms for medical imaging research. Combined with previously developed pediatric phantoms, the XCAT library now has 100 models. Each phantom contains thousands of structures and is capable of modeling normal and abnormal variations in the cardiac and respiratory motions.

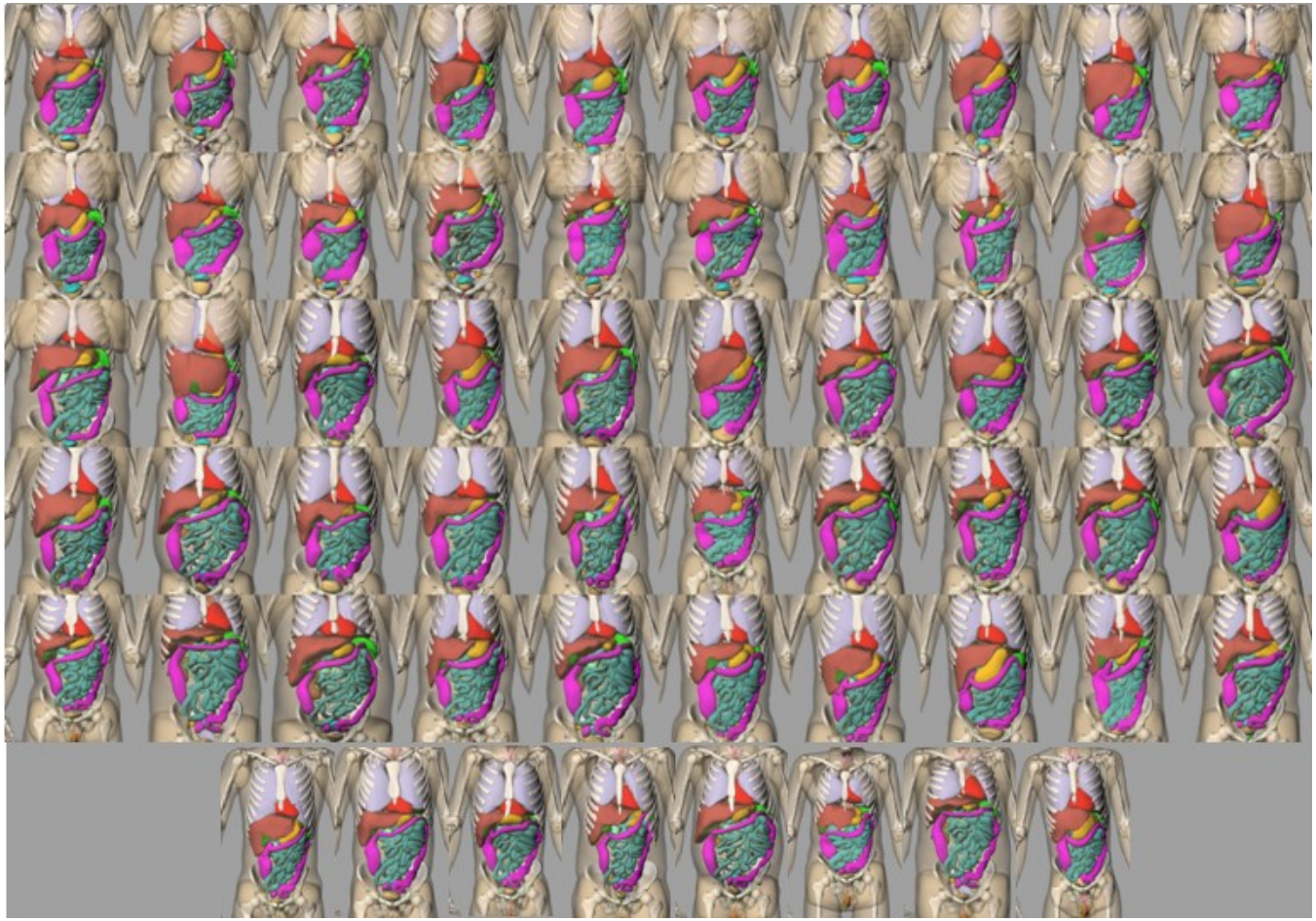

Figure 7: Collage showing the 58 new adult anatomies. The head, arms, and legs are not shown to focus on the chest-abdomen-pelvis anatomy, which is based on the patient imaging data. The muscles and blood vessels are also not shown for presentation purposes.

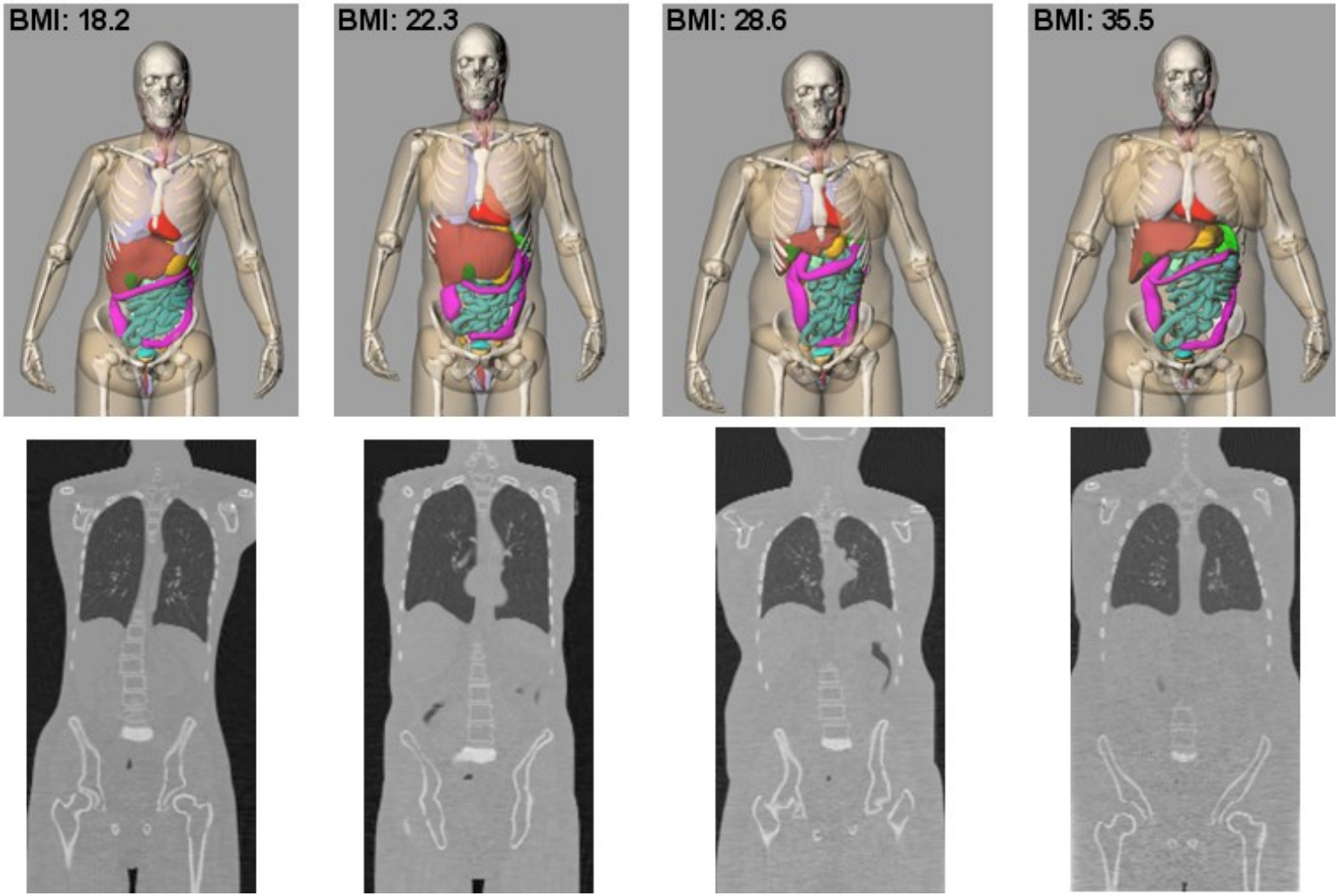

Figure 8: Four adult female XCAT phantoms (top) with CT simulation results (bottom).

With the new series of XCAT models, we now have multiple body types and sizes allowing for patient variability common of a clinical trial. Table 1 shows the mean organ masses and standard deviations from the population as compared to the standard volumes for the adult male and female from ICRP 89. As can be seen in the table, there is a great deal of variation in the organ masses (for those organs defined by CT segmentation). The mass of the breasts was found to differ the most from the ICRP values. The breasts were difficult to segment in that it was hard to determine where they end and the chest wall begins. It is possible that there is some over segmentation included in the calculated volumes. Despite that, we did find a great deal of variation in the breast masses, ranging from 300 to 3000 grams. The mean stomach mass also differed with the ICRP values, but this can be expected given the stomach volume changes a great deal depending on how much the subject ate prior to imaging. The masses for the pancreas, spleen, and gallbladder were also found to vary from the ICRP values; however, their masses did fall into the range observed in other studies[15-17].

Table 1: Mean and standard deviation of the organ masses of the adult models as compared with the organ masses from ICRP 89

	Mean Organ Mass (g)		ICRP 89 Organ Mass (g)		Percent Difference	
	Male	Female	Male	Female	Male	Female
Prostate	18.1 ± 13%		17		6%	
Testes	32.3 ± 5%		35		-8%	
Breasts		1249.0 ± 51%		500		150%
Ovaries		11.1 ± 5%		11		1%
Uterus		83.7 ± 4%		80		5%
Brain	1497.9 ± 2%	1364.4 ± 1%	1450	1300	3%	5%
Lungs[c]	1310.2 ± 23%	1036.5 ± 22%	1200	950	9%	9%
Liver	1871.5 ± 24%	1567.4 ± 18%	1800	1400	4%	12%
Pancreas	106.3 ± 34%	74.8 ± 42%	140	120	-24%	-38%
Stomach[a]	303.1 ± 47%	217.9 ± 54%	400	370	-24%	-41%
Oesophagus[b]	40.1 ± 5%	35.1 ± 5%	40	35	0%	0%
Larynx/Pharynx	31.2 ± 10%	21.9 ± 7%	28	19	11%	15%
Spleen	240.4 ± 39%	169.7 ± 38%	150	130	60%	31%
Gallbladder	33.3 ± 58%	25.1 ± 80%	68	56	-51%	-55%
Kidneys	363.5 ± 26%	298.1 ± 18%	310	275	17%	8%
Adrenals	14.9 ± 7%	13.5 ± 13%	14	13	6%	4%
Small Intestine[a]	1025.8 ± 5%	842.8 ± 15%	1000	880	3%	-4%
Large Intestine[a]	704.7 ± 3%	690.8 ± 11%	670	680	5%	2%
Bladder[b]	50.5 ± 5%	40.5 ± 5%	50	40	1%	1%
Thyroid	21.9 ± 5%	18.6 ± 1%	20	17	9%	9%
Thymus	24.4 ± 7%	19.3 ± 4%	25	20	-2%	-3%
Salivary glands	90.8 ± 3%	75.3 ± 3%	85	70	7%	8%
Pituitary	0.6 ± 0%	0.6 ± 1%	0.6	0.6	5%	5%
Eyes	15.2 ± 1%	15.5 ± 9%	15	15	1%	3%
Trachea[b]	10.1 ± 5%	8.1 ± 5%	10	8	1%	1%
Heart[c]	810.3 ± 20%	668.6 ± 20%	840	620	-4%	8%
Muscle, Skeletal	29929 ± 18%	20465 ± 8%	29000	17500	3%	17%
Skeleton, Total	10351 ± 10%	8821.7 ± 5%	10500	7800	-1%	13%
Marrow[d]	3598 ± 10%	3053 ± 5%	3650	2700	-1%	13%
Total Body (kg)	85.4 ± 19%	73.9 ± 19%	73	60	17%	23%

[a] Mass of wall and contents.

[b] Based on enclosed volume of hollow structure, where the wall thickness can be defined in the phantom program.

[c] Mass with blood.

[d] Bone marrow determined as fractional distribution of total skeleton . Alternatively, bone thickness can be specified by the user to define the amount of marrow contained within the bones.

2.4 Discussion

In this work, we created the first library of 4D computational phantoms. Our methods provided a novel and highly efficient tool, allowing the rapid development of realistic anatomically diverse 4D computational models by morphing an anatomical template. Using our techniques, it was possible to create a new patient model, containing all structures defined in the XCAT, within 3-4 days. Like most phantom development, the major bottleneck in the process was the creation of the initial patient model using segmentation. In this work, we segmented a great deal of structures to ensure accurate transforms. Using automated or semi-automated segmentation algorithms could greatly speed up this process.

The techniques used to create our phantoms are similar to those used previously to create new models by transforming existing templates[18-22]. By using segmented patient imaging data to guide our transforms, though, we capture more of the interior variability in the organ shapes and positions from patient to patient. Our models are also very highly detailed and 4D making them applicable to high-resolution 3D and 4D imaging studies. A drawback to these models is that the head, arms, and legs are still created by adding on scaled template versions. This could be overcome by using whole-body image data, as opposed to chest-abdomen-pelvis scans. Another drawback to using these phantoms for imaging studies is that the structures defining tissues and organs are assumed to be homogenous. This can lead to unrealistic appearances, most

notably a ‘cartoon’ effect for certain structures (Fig. 7), to which the remainder of this document is dedicated.

3. Part Two: Simulating anatomical texture for virtual human model

3.1 Background

In the previous section we set out to create an anatomically variable populace of phantoms. This was done by using patient CT data, so the phantoms created enjoy not only a wide variety of geometry, but that variety is realistic. This effort could enable the possibility of virtual clinical imaging trials. The drawback to this library, as mentioned earlier, is that the surfaces defining organs and structures within the body are assumed to be homogenous. This leads to unrealistic appearances when the phantoms are combined with imaging simulators, particularly with x-ray CT. In this section we seek to address this limitation of the XCAT phantoms.

The primary purpose behind developing computational models is to describe, as accurately as possible, anatomy or pathology of the body, with the intent of studying the behavior of that anatomy or pathology under controlled simulation conditions[23]. Given that current medical imaging is able to discern subtle intra-organ differences, digital imaging simulators should be developed to do the same. Hence, it is compulsory that we move forward from defining surface boundaries of organs to delineating how materials within an organ behave, i.e. incorporating tissue heterogeneity, or texture.

Incorporating realistic texture allows for qualitative studies to be conducted with virtual phantoms. For example, a textured phantom could be used to provide realistic background for lesion or disease models. Or, given a textured phantom, the effect of

imaging parameters on textural preservation could be assessed. Successful texture models contain at least two qualities; generality and realism. The texture model should be generally applicable for a variety of purposes or phantoms, yet realistic in its appearance. In this work, we sought to develop such a model for liver and lung texture in CT. To our knowledge, no work has been undertaken to synthesize anatomical texture in CT imaging. We present a method whereby patient-informed CT texture can be modeled and incorporated into computational phantoms.

3.2 Methods

The texture model was implemented into the XCAT phantom using the following four steps; texture preparation, texture extraction, texture extrapolation, and texture transfer.

3.2.1 Texture Preparation

We utilized CT image data from the Duke CT database as the source for our textures. The images were procured under IRB approval. Data were chest-abdomen-pelvic scans of adult patients, 5 mm slice thickness. In order to reduce the quantum noise entering into and contaminating the texture model, a non-linear noise reduction algorithm (anisotropic diffusion) was applied to the images. The de-noising protocol[24, 25] was a filter convolved with an image-volume. For a given 3x3x3 neighborhood, the center pixel $I_{i,j,k}$ at location (i, j) in slice k was iteratively adjusted over t steps according to the equation

$$I_{i,j,k}^{t+1} = I_{i,j,k}^{t} + \lambda[c_N * \nabla_N I + c_S * \nabla_S I + c_E * \nabla_E I + c_W * \nabla_W I + c_U * \nabla_U I + c_D * \nabla_D I]_{i,j,k}^{t}, \quad [1]$$

where λ is a constant with range of $0 \leq \lambda \leq ¼$; *N, S, E, W, U, D*, indicate North, South, East, West, Up, and Down neighbors from the center pixel in the 3x3x3 neighborhood; ∇ is the intensity difference between the center pixel $I_{i,j,k}$ and its nearest-neighbors; and $c_{...}$ is the conductivity coefficient. $c_{...}$ is calculated by

$$c_{...} = \frac{1}{1+\left(\frac{\|\nabla I\|}{\kappa}\right)^2}, \quad [2]$$

where κ is a user-defined constant. By inspection, it is noted that neighborhood smoothing was weighted inversely with the steepness of the gradient in that neighborhood, which attempts to maintain sharp edges.

Given the interplay of noise and contrast resolution, the integrated power spectral density served as a metric for quantifying how much smoothing had been applied. The power spectral density (PSD) function was estimated by taking the squared Fourier transform of ROIs within the liver[26], or equivalently

$$PSD(u,v) = \frac{{d_{xy}}^2}{{N_{xy}}^2} * |\mathcal{F}\{I(x,y) - P(x,y)\}|^2 \ , \qquad [3]$$

where u and v are spatial frequencies (1/mm) in x and y directions, d_{xy} is the pixel size (mm), N_{xy} is ROI size, $\mathcal{F}\{\ \}$ is the two-dimensional (2D) Fourier transform, $I(x,y)$ is the pixel intensity (HU) of a ROI at position (x,y), and $P(x,y)$ is a 2nd degree polynomial fit of $I(x,y)$. The subtraction was made to remove any direct-current (DC) component and reduce low frequency non-uniformities[26-28]. A one-dimensional (1D) representation of the PSD was calculated by averaging six adjacent columns about the center line of frequency space in the y direction[26].

Since PSD measurements were noisy, the 1D PSD was calculated for multiple ROIs (32 x 32 pixels, as many non-overlapping ROIs could fit inside the liver). For each set of images, the PSD was taken as the average across this ensemble of ROIs. The standard deviation (SD) was computed across all 1D PSD estimates within the ensemble. The SD represents the shaded error bands shown in Figure 9.

The images were smoothed until the 1D PSD was reduced to 50% (see Fig. 9). Since the liver volume varied considerably between patients, there was variability in the total number of ROIs that were used for PSD measurements. Once the de-noising was applied, the images were ready for texture extraction.

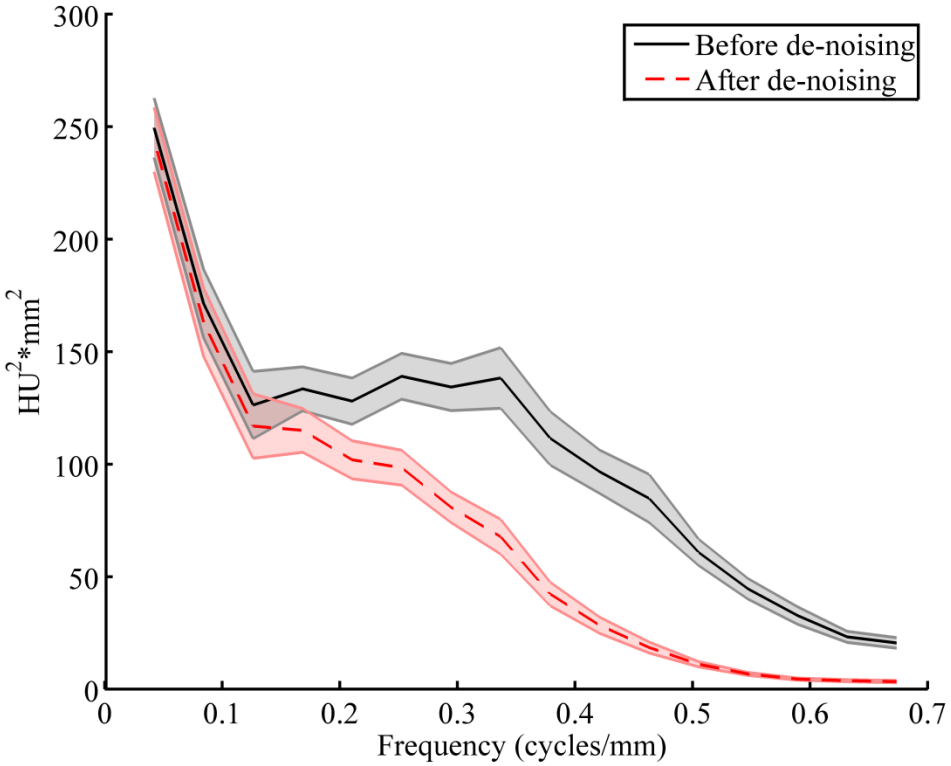

Figure 9: Using a diffusion technique, the patient images were smoothed until the power spectra density in the liver was reduced to 50%.

3.2.2 Texture Extraction

The texture extraction was accomplished by horizontally aligning several ROIs taken from the organs of interest (for each model: liver = 30 ROIs 30x30 pixels; lungs = 45 ROIs 25x25 pixels). The purposes behind creating a tiled image from multiple ROIs are twofold. First the texture synthesis algorithm (described in 3.2.4) accepted as input a

singular 2D image. Second, because the algorithm accepts only one image, it was necessary that the input image be large enough to produce unique results.

When selecting ROIs to build the input image, care was taken to avoid larger structures which are already included in the XCAT phantoms such as the blood vessels or early generations of lung bronchi, which is why ROIs from the lungs were smaller than those from the liver. It was also imperative that there should be some level of similarity between neighboring ROIs in order to avoid interference in the texture synthesis stage. For instance, two adjacent ROIs with grossly different intensities between their edges would be avoided, while ROIs with similar pixel values between their edges would be sought after. This was ensured by visually comparing ROIs once they were tiled together. Shown in Figure 10 is an example with multiple ROIs taken from a prepared lung CT image. The texture was taken from both the lungs and liver of ten clinical patients.

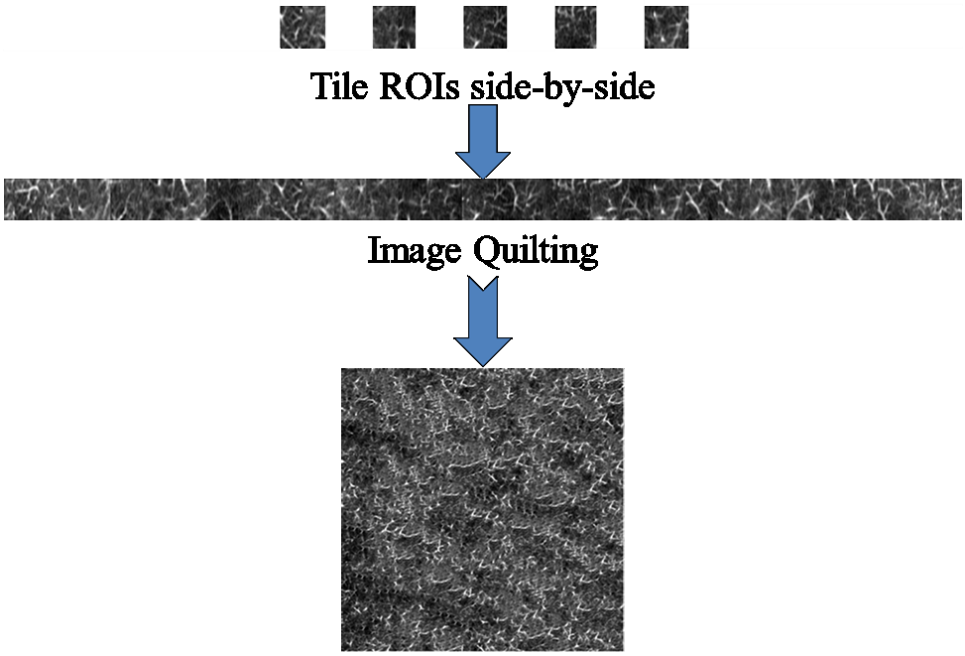

Figure 10: An ensemble of ROIs taken from CT images of a patient's lung serves as input for the Image Quilting algorithm which was used to create textures.

3.2.3 Texture Extrapolation

A larger texture was needed to completely fill in the particular organ of interest. This required taking the small ROI ensemble and extrapolating the image to a larger field. Since the standard CT image is 512x512 pixels, the textures were extrapolated to this size to generate sufficient "real texture". This was accomplished by using Image Quilting, a popular algorithm in the computer graphics community developed by Efros & Freeman [29]. What follows is a brief overview of the algorithm.

Given the smaller texture source, a larger texture was generated from the following steps: First, the algorithm divided the source texture into blocks as defined by the user. Here, the blocks were defined as 8 x 8 pixel squares. The overlap regions, also

user defined, were the outer three rows & columns of the ROIs. Next, a block was selected at random and a second block was picked that was similar to the first.

Block similarity was estimated by calculating the cross-correlation of the overlap regions between the first block and the remaining blocks. The second block was chosen at random from the 10% most similar blocks. Then the two blocks were overlapped, and the overlap was trimmed along the line of the most similar pixel pairs, essentially 'stitching' the two blocks together. Finally, this process was repeated in raster fashion until a larger texture image was created (Figure 11).

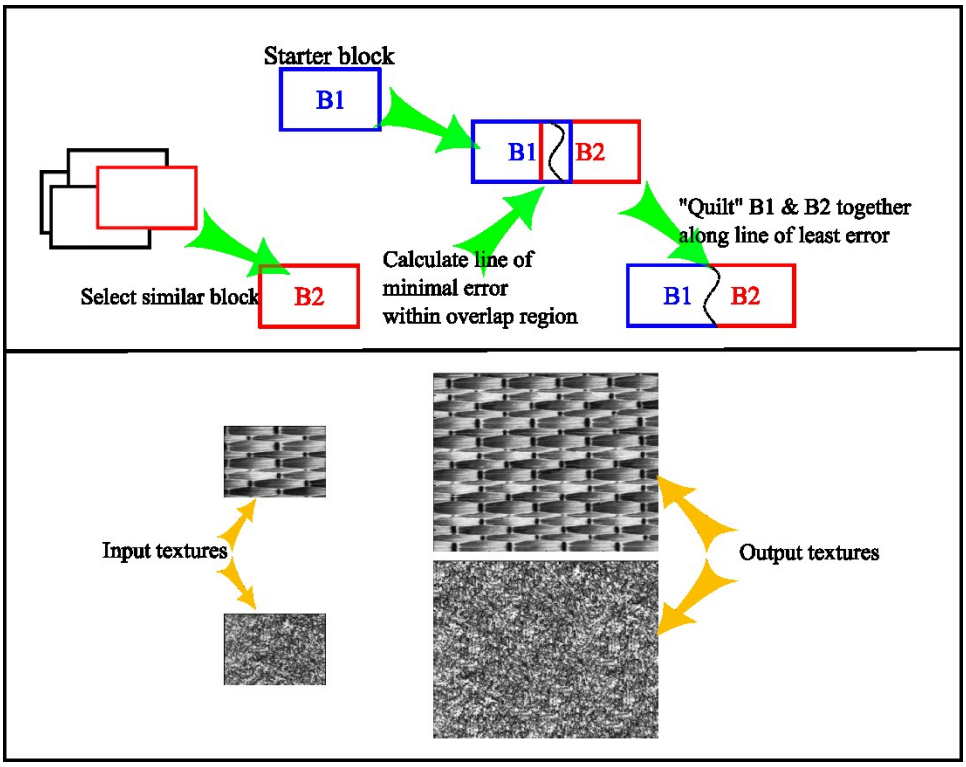

Figure 11: Top - The Image Quilting algorithm is graphically illustrated. Bottom - Larger images can be generated from a smaller sized texture source.

3.2.4 Texture Transfer

For this investigation, we used the standard adult male XCAT phantom that was 50th percentile in height and weight. The XCAT phantom was voxelized at the same resolution as the patient CT images used to provide the textures. The organs and structures were filled with typical Houndsfield Unit (HU) values. Since the extrapolated textures and the voxelized phantoms had the same pixel resolution and the same dimensions, the voxels in the phantom lung and liver were directly replaced with the corresponding texture pixels (Figs. 12, 13).

Figure 12: Once a large texture image is generated, it is combined with a voxelized XCAT phantom to produce a more realistic appearing model.

3.2.5 Phantom Simulation

CT projection data was simulated from the textured phantoms using an analytical x-ray projection algorithm in MATLAB. Poisson noise was added to the projections to ensure comparable noise appearance between the reconstructions and patient CT data. The projection data was reconstructed using a standard filtered backprojection (FBP) algorithm with a Hamming window.

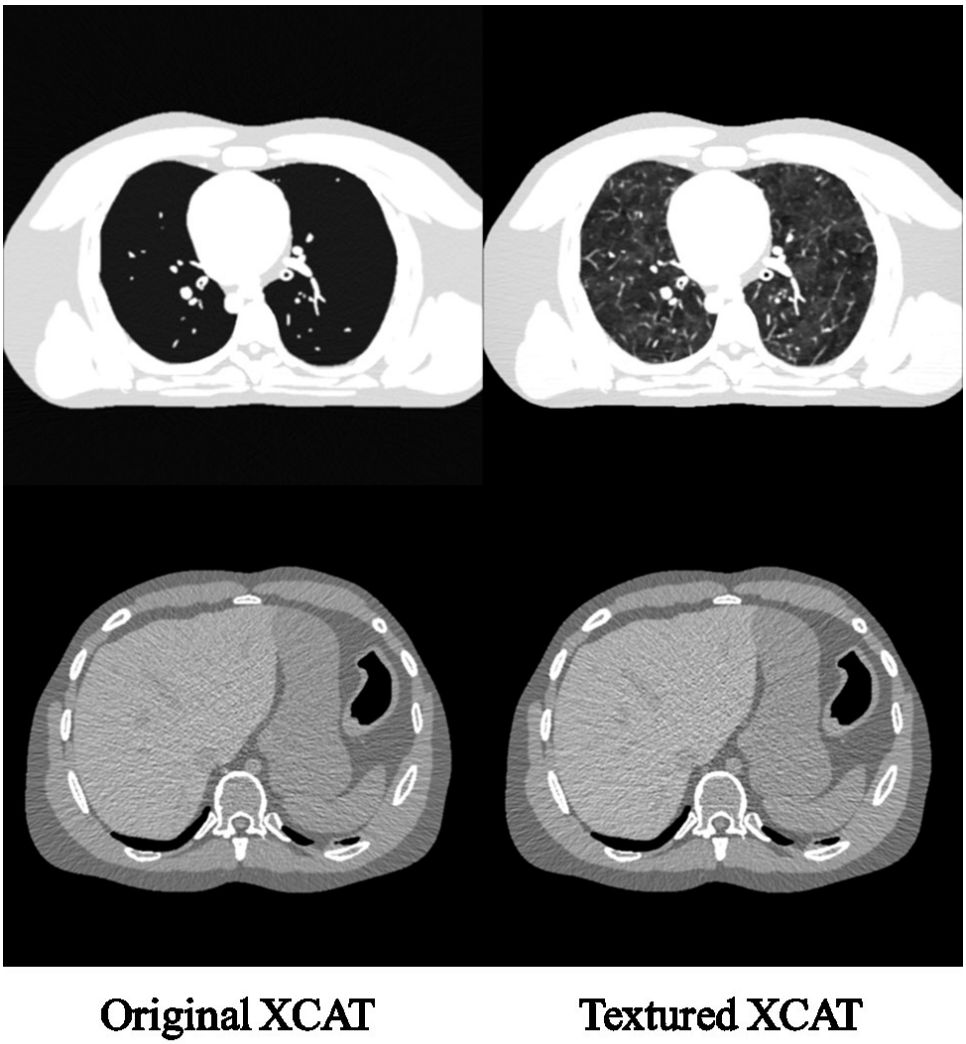

Figure 13: Using our methods, computational phantoms can move from surface defined structures (left) to filling in structures with patient-informed texture (right).

3.2.6 Texture Evaluation

Texture ROIs of various sizes (30x30 up to 60x60 pixels) from both clinical images and the simulated images (30 simulated, 30 real, from both organs; 30x2 + 30x2 = 120 ROIs) were used in an observer study with 5 experienced radiologists (Figure 14). Observers could review previous images if desired and were given no time limit to

complete the study. They were asked to rate the realism of each image on a scale of 1 (appearing simulated) to 10 (appearing real).

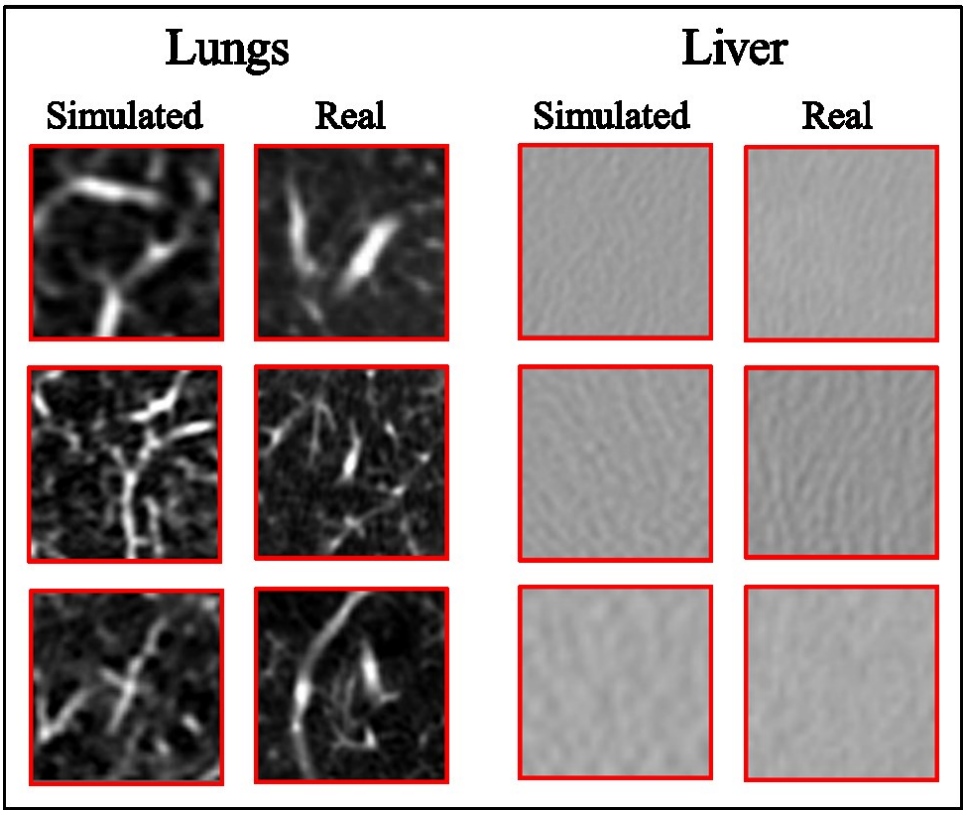

Figure 14: ROIs of different sizes were displayed at 120x120 pixels before observers. Left, lung textures from simulated and real cases are displayed. Right, liver textures from simulated and real cases are shown.

Four characteristics were used to evaluate the textures, adapted from a previously published framework[30]. First, a two-sample t-test (significance level at 0.05) was used for each observer to compare the difference of mean scores between the real and simulated textures, $\Delta\bar{\mu}$. Second, a receiver operating characteristic (ROC) analysis was performed. The area under the ROC curve (AUC) was employed as a metric for texture realism. An AUC of 0.5 would show that observers are rating the simulated and

real textures equivalently, implying that the simulated and real textures are visually indistinguishable. Further, an equivalence test was performed using 95% confidence intervals of $\Delta\bar{\mu}$, with a zone of equivalence defined as $\pm\langle\sigma_{\text{real}}\rangle$, the standard deviation of real texture scores averaged across observers. Finally, the differences of average scores between real and simulated textures were used to ascertain the degree of similarity. These tests were performed for each texture type and each observer individually. All statistical measures were performed within MATLAB.

3.3 Results

3.3.1 T-tests

Examples of the XCAT phantom with inserted texture are given in Figure 13. Compared to the lung texture, the liver texture was not as discernible due to the noise in the images. Results from the t-tests are summarized in Table 1. For the liver, in all but one case, the mean score differences between real and simulated textures were not statistically significant. For the lungs, in roughly half of the cases there was not a statistically significant difference. For the second observer, the mean score differences for lung texture was *nearly* significant, given that 0.0531 is very close to the 0.05 *p*-value threshold.

3.3.2 ROC analysis

The ROC curves and AUC measures from observer responses are summarized in Figure 15 and Table 3. Considering all observers, the AUC for the lung and liver textures were 0.67 and 0.53, respectively. The ROC analysis is used to demonstrate the efficacy of discriminating between two datasets. An AUC of 1.0 would imply that the observer(s) could correctly discern between 'true' results and 'false' results without error. In conventional use of ROC, the discrimination is between the presence and the absence of a lesion. For this work, the discrimination was in terms of real and simulated. It was hoped that observers would *not* be able to segregate real and simulated textures. Hence, an AUC that approached 0.5 was the goal.

In some instances with the liver textures, the ROC curve dipped below the chance line. This was due to observers rating the simulated textures higher than the real textures. For the liver textures, observer responses spread considerably around the target 'chance line'. The likely causes of this variation are due to intra- and inter-observer variability. With a larger pool of observers and increased number of sample textures, this variation would be reduced.

For the lung textures, radiologists' responses clustered above the 'chance line', indicating that they rated real textures with high scores more frequently than artificial textures with high scores. However, the curves from the lung textures were still closer to the chance line than they were to the upper-left corner; implying that the simulated lung textures were only moderately distinguishable from real lung textures.

Table 2: Summary of t-test results comparing mean scores of simulated and real textures. The threshold of significance was 0.05; below which, results were considered statistically significant.

	Observer	Real	Simulated	$\Delta\bar{\mu}$	Significant?	*p*-value
Lung ROIs	1	7.17±1.70	6.17±1.32	1.00	Yes	0.0161
	2	5.38±2.41	4.27±1.77	1.11	Nearly	0.0531
	3	7.03±1.99	5.13±1.71	1.90	Yes	2.97E-04
	4	5.66±1.88	5.07±1.21	0.59	No	0.168
	5	7.62±0.61	7.20±0.54	0.42	Yes	0.0081
	All	6.58±1.31	5.35±0.94	1.23	Yes	1.82E-04
Liver ROIs	1	4.21±1.79	4.50±1.88	-0.29	No	0.5483
	2	5.41±2.03	6.27±1.81	-0.85	No	0.0994
	3	5.69±1.51	5.00±1.44	0.69	No	0.0886
	4	6.52±1.00	5.83±0.93	0.68	Yes	0.0101
	5	4.82±0.85	4.90±1.14	-0.08	No	0.7694
	All	5.10±1.13	5.16±0.89	-0.06	No	0.8248

Table 3: The area under the ROC curve (AUC) served as a metric for realism. An AUC value of 0.5 implies that simulated textures were indistinguishable from real textures.

AUC		
	Lungs	Liver
Observer 1	0.6879	0.4711
Observer 2	0.6333	0.3877
Observer 3	0.7603	0.6424
Observer 4	0.6069	0.6808
Observer 5	0.6667	0.4483
Average	0.6710	0.5261

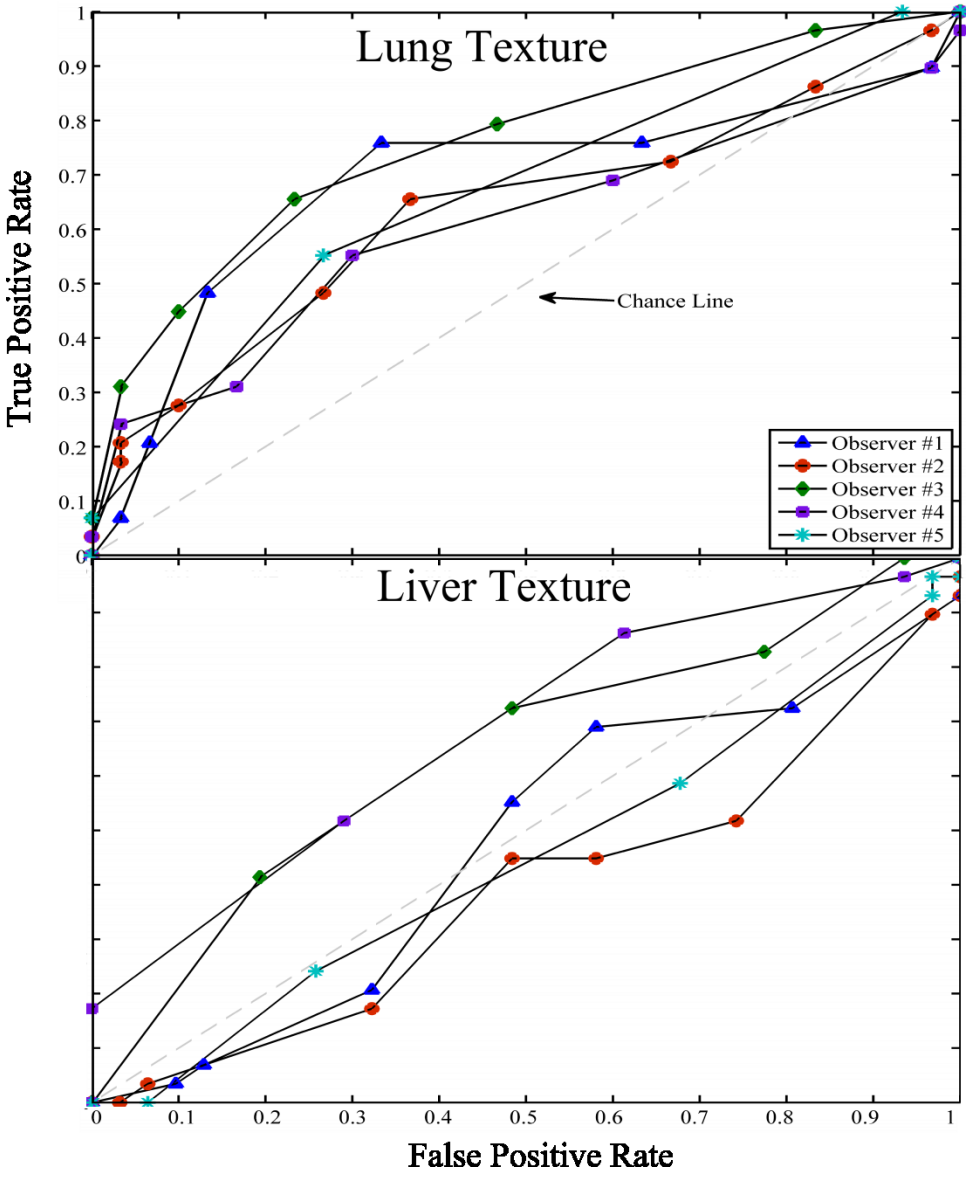

Figure 15: Results of the receiver operator (ROC) analysis showing true positive rate plotted against false positive rate. Textures from real patients were considered positive cases. Responses from lung textures are above and liver textures are below.

3.3.3 Equivalence tests

The results of the equivalence tests are given in Figure 9. The 95% confidence interval of $\Delta\bar{\mu}$ was within the equivalence zone half of the time for both lungs and liver.

Taking the total width of $\Delta\bar{\mu} \pm 95\%$ into consideration, the majority of the confidence intervals were included within the equivalence zone. In half of the instances did portions of the confidence intervals extend beyond the equivalence zone. And in only one case did $\Delta\bar{\mu}$ lie outside the equivalence zone. Analogous to the t-test, if the 95% confidence interval of $\Delta\bar{\mu}$ were to fall on or cross zero (dashed vertical line in Fig. 16), then the hypothesis that real textures were significantly different than fake textures would be rejected. From Figure 16, the 95% confidence interval of $\Delta\bar{\mu}$ crossed zero three times for the liver and once for the lung.

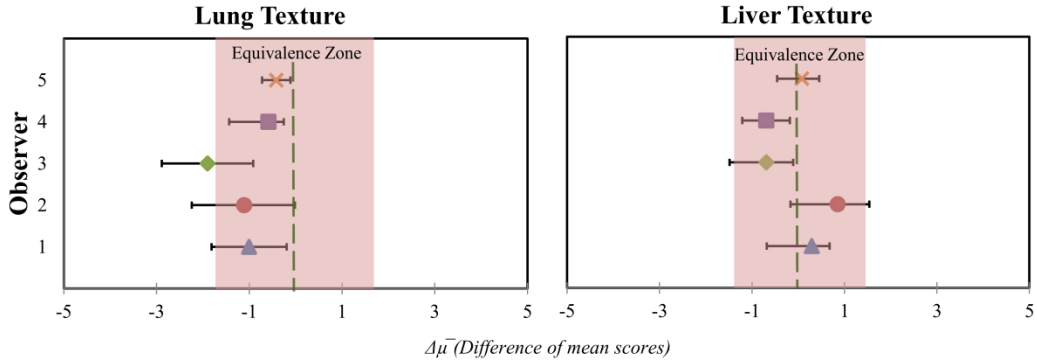

Figure 16: Results from the equivalence test based on the 95% confidence interval of $\Delta\bar{\mu}$ (difference of mean scores between real texture and artificial texture). The equivalence zone was defined as $\pm\langle\sigma_{real}\rangle$, the standard deviation of real texture scores averaged across observers.

3.3.4 Score differences

While using the above tests provide a very stringent assessment of whether or not the scores received from the textures were statistically significant, it is important to consider clinical significance. In other words, the magnitudes of the scores' differences

were used to qualitatively assess the similarity, or lack thereof between textures. In Table 2, $\Delta\bar{\mu}$ for each observer and tissue type is tabulated.

On average, the score differences between real and simulated lung texture was one, with negligible differences from the liver. The greatest disparity between real and simulated lung texture was less than two (on a scale of 1 to 10), and for the liver textures that greatest difference was 0.85. Note the negative $\Delta\bar{\mu}$ values from the liver responses; which arose from observers giving artificial textures *higher* scores than their real counterparts. These minute disparities strongly suggest that there were little clinically, or visually, significant differences between the simulated textures and the real textures.

3.4 Discussion

The focus on recent human phantom development has been accurately representing the boundaries of organs and other structures, with the assumption of uniformity therein. The exception to this is breast tissue modeling in mammography[31-33]. Phantoms that fail to assume heterogeneity within organs and structures limit their potential for providing realistic looking images from imaging simulations, especially if those heterogeneities are apparent in patient images. Tissue heterogeneities, while technically deterministic, can be modeled stochastically. Texture has also been studied as a way to classify normal tissue from diseased tissue in lungs and liver in CT[34-39].

In order to more accurately model the anatomy of the lungs and liver within CT imaging, intra-organ differences (texture) need to be modeled. This is especially true when seeking to produce realistic looking images from imaging simulators that are capable of discerning subtle intra-organ differences. To address this, we set out to create a framework whereby anatomical heterogeneities, or texture, could be modeled. While our approach could theoretically be applied to any tissue type we focused in this study on the lungs and liver textures.

As an alternative to using a stochastic process in modeling texture, one could extend the hybrid phantom approach and fit surfaces to sub-organ structures, such as fine branches of lung paranchema. The advantage of this approach would be that the

model generated is accurately based on reality. However, to do so would result in large cost in computer memory, and time with segmenting more structures.

We instead adapted an algorithm from the computer graphics industry, Image Quilting, to generate tissue textures. The risk in doing so was that structures could propagate randomly, which not only is deviant from reality but could lead to unrealistic effects. However, the advantages of our approach were that there was no additional segmentation necessary, it was memory efficient, and the stochastic nature meant that one source texture could be used repeatedly to generate multiple texture realizations.

Our assessment of the simulated textures indicated that there was no noticeable visual difference between the 'flat' untextured phantom and the textured version (Figure 7) for the liver. This could be attributed to 1) perceived texture in soft tissue is dominated by noise appearance or 2) noticeable changes in the liver are seen over larger areas or 3) a combination of 1) and 2). The texture was much more visible in regards to the lungs. For the lungs, our texture added additional anatomy (smaller branches of the pulmonary vessels and bronchial tree) that made this texture more prominent. It is important to note that this background anatomy is independent of and can add to the XCAT's existing model for the pulmonary vessels and airway tree.

Generality of our texture simulation was demonstrated in that the framework was applied to two visually different organs from ten different patients. While only one

phantom was used to house this texture, this approach is compatible with any voxelized phantom.

Determining how well the synthetic textures resembled reality was a major focus of this work. Realism was rigorously assessed with three tools; ROC analysis with AUC measurements, a significance test (statistical and clinical), and equivalence testing. Based on the AUC measurements, the synthetic liver textures were indistinguishable from the real liver textures. That same metric suggested however that observers could tell with some consistency which lung textures were real and which were artificial. Results of the other tests indicated that the realism of the synthesized and real liver textures were the same.

While it cannot be said for certain that the artificial lung textures are indistinguishable from real lung textures, there is reason to be optimistic. The top performing observer could distinguish correctly 66% of the real lung textures but would be in error 23% of the time in doing so. More importantly, the realism scores for real and simulated textures were very similar, indicative of their high degree of realism.

This preliminary work lays a foundation for adding clinically informed texture to computational phantoms. This framework was limited by a few key points. First, the de-noising protocol did not discriminate between anatomical texture and quantum noise texture, which resulted in loss of low-contrast fibrous branches of the lungs and a lack of

thin spindly objects (Figure 13). With a different de-noising approach one may be able to successfully preserve even the low-contrast objects.

Second, the images were simulated using analytical projection/reconstruction. Ideally, the textured phantoms should be simulated under conditions that match that of the patients' CT scans. This way, texture variation due to the image acquisition process could be kept minimal. Variations of this sort would be most noticeable across areas of uniformity, such as soft tissue (in our case, the liver). However, the results presented here indicate that, even given the difference between reconstructions, our simulated liver textures compared favorably with patient data, so gains to be had in this application with more elaborate simulation methods are debatable. As it was, the CT simulation methods resulted in comparable between real and simulated liver textures.

Third, since voxelized data was used for modeling texture, the XCAT phantom had to be voxelized to match the texture resolution, which led to minor sampling errors. One of the key features of the XCAT phantom is that since it is mathematically defined, the phantoms can enjoy high resolution representation, which was potentially degraded in this process. This could be overcome by creating the texture in a non-voxelized format.

Finally, there was disagreement between observer responses to the textures. In Figure 15 there is considerable spread between observers ROC curves, and for a few observers, their ROC curve flucuated dramatically; suggesting both inter- observer

variation and intra- observer variation. With only five observers and 120 cases, the t-tests and the equivalence tests were highly susceptible to these variations, making it difficult to definitively ascertain the statistical significance of texture differences. Clearly, a larger study would be needed to reduce the statistical uncertainties. However, given that the $\Delta\bar{\mu}$ values were consistently minute between all observers, a larger study would likely have marginal impact towards establishing the clinical difference between real and simulated textures.

Despite these limitations, the textured phantom images are certainly more realistic than the current state of the art computational phantoms which are completely homogenous within a given organ. As further improvements are made to modeling tissue texture, computational phantoms will move closer to being useful for image quality studies.

4. Conclusions

With the rise of computer simulation in imaging research, a population of phantoms that includes a range of anatomical variations representative of the public at large is needed to more closely mimic a clinical study or trial. The series of anatomically variable phantoms developed in this work provide a valuable resource for investigating different imaging devices and the effects of anatomy and motion in imaging. With recent advances towards more volumetric and dynamic imaging, the phantoms have enormous potential to study the effects of anatomical, physiological, physical, and instrumentational factors on imaging and to research new image acquisition strategies, image processing and reconstruction methods, and image visualization and interpretation techniques. The phantoms can be used to simulate any number of different situations using various imaging applications (CT, MRI, ultrasound, SPECT, PET) and scanning parameters (spatial and temporal resolution, dose, kVp, radiopharmaceutical, etc).

Combined with accurate Monte Carlo dose estimation programs, the phantom series will also provide the necessary foundation to optimize imaging applications in terms of image quality and radiation dose and to enable patient-specific estimation of dose and radiation risk. With a library of anatomies to choose from, better matches may be found for a particular patient that would enable more accurate prospective estimation of patient-specific organ and effective dose. Future work will include further expansion

of this library, ultimately to a population of hundreds of phantoms ranging in age from newborn to adult. Such a large compilation of phantoms will provide a great research tool for the imaging community.

This work also presents a first attempt at incorporating patient-informed CT texture into voxelized computational phantoms. We created a framework that can be compatible with any voxelized phantom. With this framework, artificial texture was generated that was comparable with patient data. This methodology proved promising toward generating realistic anatomical texture. We plan to further exploit this framework for implementing more anatomical textures into computational phantoms in parametric modeling and generating 3D textures.

References

1. Segars W, Bond J, Frush J, Hon S, Eckersley C, Williams CH, Feng J, Tward DJ, Ratnanather TJT, Miller MI, Frush D, Samei E. Population of anatomically variable 4d xcat adult phantoms for imaging research and optimization. *Medical Physics*. 2013;40:043701

2. Bond J, Frush J, Hon S, Eckersley C, Williams CH, Feng J, Tward DJ, Ratnanather TJT, Miller MI, Frush D, Samei E, Segars WP. Series of 4d adult xcat phantoms for imaging research and dosimetry. 2012:83130P-83130P

3. Bond J, Frush D, Samei E, Segars W. Simulation of anatomical texture in voxelized xcat phantoms. *SPIE Medical Imaging*. 2013:86680N-86680N-86686

4. Segars W, Mahesh M, Beck T, Frey E, Tsui B. Realistic ct simulation using the 4d xcat phantom. *Medical physics*. 2008;35:3800

5. Tang J, Hall N, Rahmim A. Mri assisted motion correction in dual-gated 5d myocardial perfusion pet imaging. *IEEE Nuclear Science Symposium Conference Record*. 2012

6. Buck AK, Herrmann K, Stargardt T, Dechow T, Krause BJ, Schreyögg J. Economic evaluation of pet and pet/ct in oncology: Evidence and methodologic approaches. *Journal of Nuclear Medicine Technology*. 2010;38:6-17

7. Chun S, Fessler J, Dewaraja Y. Correction for collimator-detector response in spect using point spread function template. 2012

8. Mishra P, Li R, St James S, Mak RH, Williams CL, Yue Y, Berbeco RI, Lewis JH. Evaluation of 3d fluoroscopic image generation from a single planar treatment image on patient data with a modified xcat phantom. *Physics in medicine and biology*. 2013;58:841

9. Caon M. Voxel-based computational models of real human anatomy: A review. *Radiation and environmental biophysics*. 2004;42:229-235

10. Segars W, Sturgeon G, Mendonca S, Grimes J, Tsui B. 4d xcat phantom for multimodality imaging research. *Medical physics*. 2010;37:4902

11. Li X, Samei E, Segars WP, Sturgeon GM, Colsher JG, Toncheva G, Yoshizumi TT, Frush DP. Patient-specific radiation dose and cancer risk estimation in ct: Part ii. Application to patients. *Medical physics*. 2011;38:408

12. Beg MF, Miller MI, Trouvé A, Younes L. Computing large deformation metric mappings via geodesic flows of diffeomorphisms. *International Journal of Computer Vision*. 2005;61:139-157

13. Joshi SC, Miller MI. Landmark matching via large deformation diffeomorphisms. *Image Processing, IEEE Transactions on*. 2000;9:1357-1370

14. Ceritoglu C. Multichannel large deformation diffeomorphic metric mapping and registration of diffusion tensor images. 2008

15. de la Grandmaison GL, Clairand I, Durigon M. Organ weight in 684 adult autopsies: New tables for a caucasoid population. *Forensic science international*. 2001;119:149

16. Kishk S, Darweesh R, Dodds WJ, Lawson TL, Stewart ET, Kern M, Hassanein E. Sonographic evaluation of resting gallbladder volume and postprandial emptying in patients with gallstones. *American Journal of Roentgenology*. 1987;148:875-879

17. Çerçi SS, Özbek FM, Çerçi C, Baykal B, Eroğlu HE, Baykal Z, Yıldız M, Sağlam S, Yeşildağ A. Gallbladder function and dynamics of bile flow in asymptomatic gallstone disease. *World journal of gastroenterology: WJG*. 2009;15:2763

18. Ding A, Mille MM, Liu T, Caracappa PF, Xu XG. Extension of rpi-adult male and female computational phantoms to obese patients and a monte carlo study of the effect on ct imaging dose. *Phys. Med. Biol.*;57

19. Johnson PB, Whalen SR, Wayson M, Juneja B, Lee C, Bolch WE. Hybrid patient-dependent phantoms covering statistical distributions of body morphometry in the us adult and pediatric population. *Proceedings of the IEEE*. 2009;97:2060-2075

20. Na YH, Zhang B, Zhang J, Caracappa PF, Xu XG. Deformable adult human phantoms for radiation protection dosimetry: Anthropometric data representing size distributions of adult worker populations and software algorithms. *Phys. Med. Biol.*;55:3789-3811

21. Cassola VF, Milian FM, Kramer R, de Oliveira Lira CAB, Khoury HJ. Standing adult human phantoms based on 10th, 50th and 90th mass and height percentiles of male and female caucasian populations. *Phys. Med. Biol.*;56:3749-3772

22. Broggio D, Beurrier J, Bremaud M, Desbree A, Farah J, Huet C, Franck D. Construction of an extended library of adult male 3d models: Rationale and results. *Phys. Med. Biol.*;56:7659-7692

23. Zaidi H, Tsui BMW. Review of computational anthropomorphic anatomical and physiological models. *Proceedings of the IEEE*. 2009;97:1938-1953

24. Catté F, Lions PL, Morel JM, Coll T. Image selective smoothing and edge detection by nonlinear diffusion. *SIAM Journal on Numerical Analysis*. 1992;29:182-193

25. Perona P, Malik J. Scale-space and edge detection using anisotropic diffusion. *Pattern Analysis and Machine Intelligence, IEEE Transactions on*. 1990;12:629-639

26. Dobbins III JT, Samei E, Ranger NT, Chen Y. Intercomparison of methods for image quality characterization. Ii. Noise power spectrum. *Medical physics*. 2006;33:1466

27. Boedeker KL, Cooper VN, McNitt-Gray MF. Application of the noise power spectrum in modern diagnostic mdct: Part i. Measurement of noise power spectra and noise equivalent quanta. *Physics in Medicine and Biology*. 2007;52:4027

28. Wagner RF, Brown DG, Pastel MS. Application of information theory to the assessment of computed tomography. *Medical physics*. 1979;6:83

29. Efros AA, Freeman WT. Image quilting for texture synthesis and transfer. *Proceedings of the 28th annual conference on Computer graphics and interactive techniques*. 2001:341-346

30. Li X, Samei E, Delong D, Jones R, Gaca A, Hollingsworth C, Maxfield C, Carrico C, Frush D. Three-dimensional simulation of lung nodules for paediatric multidetector array ct. *British Journal of Radiology*. 2009;82:401-411

31. Castella C, Kinkel K, Descombes F, Eckstein MP, Sottas P-E, Verdun FR, Bochud FO. Mammographic texture synthesis: Second-generationclustered lumpy backgrounds using agenetic algorithm. *Opt. Express*. 2008;16:7595-7607

32. Bochud F, Abbey C, Eckstein M. Statistical texture synthesis of mammographic images with super-blob lumpy backgrounds. *Opt. Express*. 1999;4:33-42

33. Berks M, Taylor C, Rahim R, Boggis C, Astley S. Modelling structural deformations in mammographic tissue using the dual-tree complex wavelet.

Proceedings of the 10th international conference on Digital Mammography. 2010:145-152

34. Gangeh M, Sørensen L, Shaker S, Kamel M, Bruijne M. Multiple classifier systems in texton-based approach for the classification of ct images of lung. In: Menze B, Langs G, Tu Z, Criminisi A, eds. *Medical computer vision. Recognition techniques and applications in medical imaging*. Springer Berlin Heidelberg; 2011:153-163.

35. Xu R, Hirano Y, Tachibana R, Kido S. Classification of diffuse lung disease patterns on high-resolution computed tomography by a bag of words approach. In: Fichtinger G, Martel A, Peters T, eds. *Medical image computing and computer-assisted intervention – miccai 2011*. Springer Berlin Heidelberg; 2011:183-190.

36. Sluimer IC, Prokop M, Hartmann I, Ginneken Bv. Automated classification of hyperlucency, fibrosis, ground glass, solid, and focal lesions in high-resolution ct of the lung. *Medical Physics*. 2006;33:2610-2620

37. Bharathi VS, Ganesan L. Orthogonal moments based texture analysis of ct liver images. *Pattern Recognition Letters*. 2008;29:1868-1872

38. Mougiakakou SG, Valavanis I, Nikita KS, Nikita A, Kelekis D. Characterization of ct liver lesions based on texture features and a multiple neural network classification scheme. *Engineering in Medicine and Biology Society, 2003. Proceedings of the 25th Annual International Conference of the IEEE*. 2003;2:1287-1290 Vol.1282

39. Zhao CG, Cheng HY, Huo YL, Zhuang TG. Liver ct-image retrieval based on gabor texture. *Engineering in Medicine and Biology Society, 2004. IEMBS '04. 26th Annual International Conference of the IEEE*. 2004;1:1491-1494